Finding direct correlation functions for desired two-dimensional lattices with a phase-field crystal

Ruho Kondo*
Toyota Central R&D Labs., Inc., 41-1, Yokomichi, Nagakute, Aichi 480-1192, Japan

(Received 5 January 2021; revised 29 April 2021; accepted 14 July 2021; published 27 July 2021)

The phase-field crystal model is one of the most successful models with which to describe crystallization at a near-atomic scale with a larger timescale compared with other atomistic methods when direct correlation functions (DCFs) for the desired lattice are specified. However, the DCFs are, in general, not known and are hard to obtain from essential material information, such as primitive lattice vectors and atom positions. In this paper, we propose a method of obtaining two-point DCFs for desired two-dimensional lattices. The proposed optimization scheme is simple in that it minimizes the temporal change in free energy with respect to the target lattice using a gradient descent. In numerical experiments, we successfully obtained DCFs not only for well-known two-dimensional lattices (i.e., triangular, square, rectangular, honeycomb, and kagome lattices) but also for five nontrivial lattices (i.e., maple leaf, ladybug, trellis, Lieb, and CaVO lattices). We also show that these five lattices can be simulated using a phase-field crystal with at least five modes.

DOI: 10.1103/PhysRevB.104.014112

I. INTRODUCTION

Phase-field crystal (PFC) modeling [1–3] is one of the most successful methods of representing the dynamics of crystallization at a near-atomic scale with a larger timescale compared with other atomistic methods, such as the use of molecular dynamics. The PFC model was introduced as a Swift–Hohenberg–type equation [1,2] and then connected the classical density functional theory [3]. The governing equation of the PFC model, namely, the PFC equation, is a partial differential equation derived by variational differentiation of a free-energy functional that is parametrized by n-point direct correlation functions (DCFs). Once DCFs are specified, the crystallization can be simulated by solving the PFC equation. In other words, the DCFs include all information about the crystal lattice structure and its formation process. The method is based on a free-energy principal, and the stabilities of different crystals can thus be compared when deciding the synthesizability of the crystals.

Previous studies showed that the PFC can represent various three-dimensional (3D) and two-dimensional (2D) crystal lattices, such as body-centered cubic, face-centered cubic, simple cubic, and hexagonal close-packed [4,5] and diamond-cubic [6] 3D lattices, and triangular and square [4], rectangular, honeycomb and kagome [7], and graphene [8] 2D lattices. Although the DCFs for simple lattices, such as the triangular and square lattices, can be easily determined using a method described in the literature [4,5], the atomic density within the plane is required to determine the values of DCFs. These values are easily calculated in the case of triangular and square lattices because all the plane waves constructing these lattices have peaks at the positions of atoms. In the case of the triangular lattice, for example, the atomic density within the plane corresponding to the reciprocal lattice vector $\mathbf{k}_1$ is $1/A$, where A is the lattice constant. Figure 1 (left) clearly shows that atoms are located at the peaks of the plane wave corresponding to $\mathbf{k}_1$ and the spacing between the atoms is $1/A$ on this plane. The atomic density within the plane in the case of square lattices is easily calculated according to Fig. 1 (center). In the case of other lattices (e.g., the honeycomb lattice), the atomic density within each plane is hard to determine because the atoms are not located on the peaks of the plane waves [Fig. 1 (right)]. That is to say, there is no oracle in which DCFs represent a more complicated crystal lattice. Such difficulty limits the use of the PFC model for a wide range of crystal lattice structures.

The problem considered here is stated as how to obtain an optimal DCF for the desired lattice only from the crystallographic information. We here define the crystallographic information as primitive vectors and atom coordinates of the lattice, which are included in a crystallographic information file [9]. No other information is considered. One simple approach adopted to solve this problem is minimizing the mismatch between the target desired lattice and the generated lattice, where the latter is obtained by time integrating the PFC equation. Here, the time integration is carried out until a steady state is reached. The optimal DCF is then defined as the DCF that minimizes the mismatch. This approach seems well suited to the problem considered but repeatedly calculating both the steady state and the sensitivity of the DCF for the mismatch during the optimization process requires extremely large computational resources. Reduction of the computational cost is essential to obtaining a solution in reasonable time.

In this paper, we convert the vanilla optimization problem mentioned above into a computationally less expensive problem. For further cost reduction, we propose a method of approximating target lattices using low-pass filtering. Adopting the proposed method, many types of 2D lattices, including

*r-kondo@mosk.tytlabs.co.jp

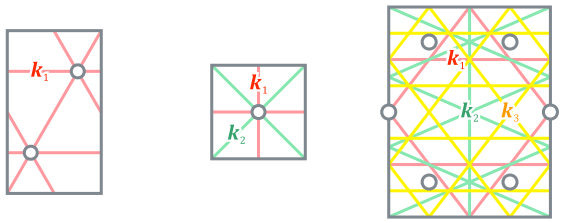

FIG. 1. Triangular (left), square (center), and honeycomb (right) lattices. The atoms are indicated by open circles. The peaks of the constructed plane waves are indicated as a solid line. The corresponding wave vector is written on each line.

some not previously reported, have been successfully reproduced.

The remainder of the paper is organized as follows: Section II discusses the free-energy functional and the PFC equation used in this paper. Section III defines the problem to be solved in this paper and proposes its alternative. In addition, the approximation of the target lattice is defined. Section IV presents the experimental results. Section VI describes related works that follow a slightly different direction compared with the work in the present paper. Section VII concludes the paper.

II. PRELIMINARIES

Let $\psi(\mathbf{r}) \in \mathbb{R}$ and $C_2(\mathbf{r}, \mathbf{r}') \in \mathbb{R}$ be an order parameter at position $\mathbf{r} \in \mathbb{R}^2$ and a two-point DCF between positions $\mathbf{r}$ and $\mathbf{r}'$, respectively. Assuming (i) the diffusion coefficient does not depend on the particle density, (ii) DCFs higher than third order are absent (i.e., the Ramakrishnan–Yussoff approximation [10]), (iii) the two-point DCF only depends on the distance between two locations, $C_2(\mathbf{r}, \mathbf{r}') = C_2(|\mathbf{r} - \mathbf{r}'|)$, and (iv) $O(\psi^6)$ terms in the ideal-gas free-energy can be ignored, a free-energy functional, $F \in \mathbb{R}$, can be written as [11]

$$F[\psi] = F_{\text{ideal}}[\psi] + F_{\text{excess}}[\psi], \tag{1}$$

where F_{ideal} and F_{excess} are, respectively, the ideal-gas energy and excess energy, defined as

$$F_{\text{ideal}}[\psi] = \int_\Omega \left(\frac{1}{2}\psi^2(\mathbf{r}) - \frac{1}{6}\psi^3(\mathbf{r}) + \frac{1}{12}\psi^4(\mathbf{r}) \right) \mathrm{d}\mathbf{r}, \tag{2}$$

$$F_{\text{excess}}[\psi] = -\frac{1}{2}\int_\Omega C_2(|\mathbf{r} - \mathbf{r}'|)\psi(\mathbf{r})\psi(\mathbf{r}')\mathrm{d}\mathbf{r}'\mathrm{d}\mathbf{r}. \tag{3}$$

Here, Ω is an unit-cell region. Assuming $\int_\Omega \psi(\mathbf{r})\mathrm{d}\mathbf{r}$ is conserved during the processing, the time development equation of ψ is derived as

$$\frac{\partial \psi(\mathbf{r})}{\partial t} = \nabla^2 \frac{\delta F}{\delta \psi(\mathbf{r})}, \tag{4}$$

where ∇ is a differential operator with respect to $\mathbf{r}$. Substituting Eq. (1) into Eq. (4) gives

$$\frac{\partial \psi_{\mathbf{k}}}{\partial t} = -k^2 \left((1 - C_{2,\mathbf{k}})\psi_{\mathbf{k}} - \frac{1}{2}(\psi^2)_{\mathbf{k}} + \frac{1}{3}(\psi^3)_{\mathbf{k}} \right), \tag{5}$$

where $k \in \mathbb{R}_+$ is the magnitude of a wave vector $\mathbf{k} \in \mathbb{R}^2$ and $(\bullet)_{\mathbf{k}}$ denotes a Fourier transformation of $(\bullet)$ at $\mathbf{k}$ in Fourier space.

III. PROPOSED METHOD

A. Definitions of Problems

In this section, we first describe a problem to be solved in this paper. An alternative that is computationally less expensive is then defined. We consider a lattice generated from white noise by solving the PFC equation [Eq. (5)] as

$$\psi^{\text{gen}}(\mathbf{r}; C_2) := \psi_0(\mathbf{r}) + \int_0^\infty \frac{\partial \psi}{\partial t}(\mathbf{r}; C_2)\mathrm{d}t, \tag{6}$$

where ψ_0 is an initial condition defined as

$$\psi_0 \sim U([m - \eta, m + \eta]^D). \tag{7}$$

Here, U is a uniform distribution, m is the noise mean, η is the noise amplitude, and D is the number of cells for the discretized ψ. Our final goal is to find the optimal DCF, C_2, which controls the crystallization dynamics of the target lattice from white noise. The optimization problem is hence written as

$$\min_{C_2} d(\psi^{\text{gen}}(\mathbf{r}, C_2), f^{\text{relax}}(\psi^{\text{tgt}}(\mathbf{r}))), \tag{8}$$

where $d(A, B)$ is a distance function that measures the mismatch between A and B, ψ^{tgt} is an approximated target lattice defined in the next subsection, and f^{relax} maps an arbitrary pattern to the nearest PFC steady state. ψ^{tgt} is just an approximation of the target lattice and is thus not guaranteed that ψ^{tgt} is included in a set of steady states of the PFC equation. This is why f^{relax} is needed. If ψ^{tgt} is a good approximation of the target lattice, f^{relax} becomes an identity.

Solving the optimization problem, Eq. (8), is highly computationally expensive because tens of thousands of time steps are required to reach the steady state of the PFC equation from white noise. In addition, there is the problem of how to define an appropriate distance function d. To overcome these difficulties, an alternative optimization problem is considered.

From a physical viewpoint, the steady state can be interpreted as being energetically stable. This means that the temporal change in the free energy of ψ^{gen} is zero at a steady state. Therefore, the temporal change in the free energy of $f^{\text{relax}}(\psi^{\text{tgt}})$ is also required to be zero when the DCF is optimal. We thus propose an alternative optimization problem defined as

$$\min_{C_2} \left| \frac{\partial F[f^{\text{relax}}(\psi^{\text{tgt}})]}{\partial t} \right|. \tag{9}$$

Compared with the original problem [Eq. (8)], the alternative problem [Eq. (9)] is computationally less expensive because the computation of ψ^{gen} is no longer required. We argue that two issues remain in the problem expressed by Eq. (9). One is that f^{relax} is still unknown and the other is that the optimal solution of Eq. (9) only guarantees that ψ^{tgt} is a metastable state. That is to say, there is no guarantee that ψ^{tgt} can be reached from white noise by solving the PFC equation. For simplicity, f^{relax} is assumed to be the identity in this study. Despite these disadvantages, Eq. (9) empirically works well for many desired 2D lattices as shown in Sec. IV.

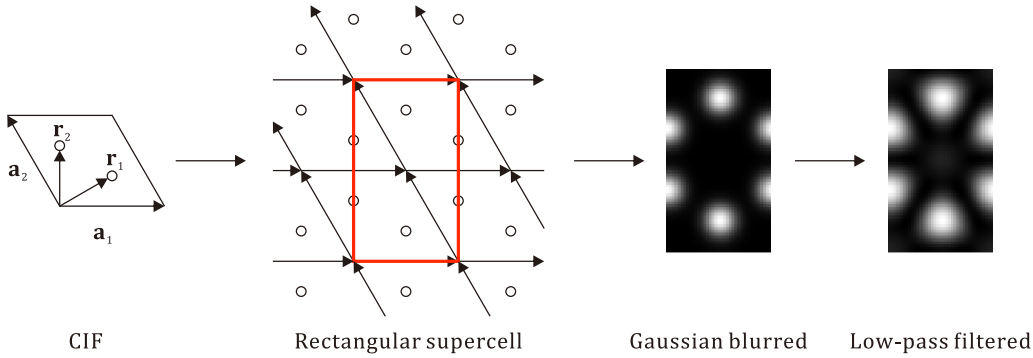

FIG. 2. Preparation steps for the target image. The rectangular supercell is extracted from an image drawn by repeatedly tiling the primitive unit cell. Each atom position is represented as a single Gaussian. The approximated target image, ψ^{tgt}, is defined as a low-pass filtered image of the Gaussian blurred image.

B. Definitions of target images

This subsection describes the method of approximating the target lattice, ψ^{tgt}. Figure 2 depicts the procedure for making the target image, ψ^{tgt}. For simplicity, we consider only the lattice whose supercell can be represented with a rectangular shape. Fortunately, various types of 2D lattices can be represented as a rectangular supercell. In addition, the rectangular supercell has good computational properties as described below.

Let $\mathbf{a}_1 \in \mathbb{R}^2$ and $\mathbf{a}_2 \in \mathbb{R}^2$ be the primitive vectors for the desired 2D lattice. The lattice vector $\mathbf{q}$ is defined as $\mathbf{q}(n_1, n_2) := n_1\mathbf{a}_1 + n_2\mathbf{a}_2 \in \mathbb{R}^2$, where $(n_1, n_2) \in \mathbb{Z}^2$. In defining the rectangular supercell, we aim to find integers n_1 and n_2 that satisfy $\mathbf{q}(n_1, n_2) = \mathbf{q}(n_1', n_2') + \mathbf{q}(n_1'', n_2'')$ and $\mathbf{q}(n_1', n_2') \cdot \mathbf{q}(n_1'', n_2'') = 0$, where $(n_1', n_2'), (n_1'', n_2'') \in \mathbb{Z}^2$ and $\mathbf{q}(n_1', n_2'), \mathbf{q}(n_1'', n_2'') \neq \mathbf{0}$, (see Fig 3). The candidate set $\mathcal{Q}$ is defined as a set of $\mathbf{q}(n_1, n_2)$ that satisfies these conditions. The rectangular supercell is defined as having a diagonal along which $\mathbf{q}^* := \mathrm{argmin}_{\mathbf{q}\in\mathcal{Q}} \|\mathbf{q}\|_2$ points, where $\| \bullet \|_2$ denotes the L_2 norm of $(\bullet)$. Note that the 3D lattice whose supercell can be represented with an orthorhombic shape can be treated in the same way as mentioned above.

After defining the rectangular supercell, the atoms are located in the cell at the atom coordinates. Here, the atoms are represented as a density field with a finite width atom-nonatom interface. Concretely speaking, a Gaussian with a covariance of $\mathrm{diag}(\sigma^2)$ is overwrapped around the coordinates of each atom,

$$\psi^{\mathrm{tgt}}(\mathbf{r}) = \sum_{j=1}^{N_{\mathrm{aotms}}} \frac{a_j}{2\pi\sigma_j^2} \exp\left(-\frac{|\mathbf{r}-\mathbf{r}_j|^2}{2\sigma_j^2}\right) \in \mathbb{R}, \tag{10}$$

where $\mathbf{r}_j \in \mathbb{R}^2$ is the position of the jth atom. The coefficient and standard deviation of each Gaussian, $a_j \in \mathbb{R}$ and $\sigma_j \in \mathbb{R}$, are the hyperparameters. Representing the atom-nonatom interface width as finite makes it easier to carry out numerical simulations such as the finite differential simulation conducted in this paper. This is because tracking the explicit position of the interface is no longer required in this representation. Instead, the position of the interface is implicitly represented as a specific value or a specific range of the density field.

In Fourier space, $\psi^{\mathrm{tgt}}(\mathbf{r})$ with a periodic condition $\psi^{\mathrm{tgt}}(\mathbf{r} + n_1\mathbf{a}_1 + n_2\mathbf{a}_2) = \psi^{\mathrm{tgt}}(\mathbf{r})$ can be written as

$$\Psi^{\mathrm{tgt}}(\mathbf{g}) = \left\{ \begin{array}{ll} \displaystyle\sum_{j=1}^{N_{\mathrm{atoms}}} a_j \exp\left(-\frac{\sigma_j^2}{2}\mathbf{g}\cdot\mathbf{g} - \mathrm{i}\mathbf{g}\cdot\mathbf{r}_j\right), & \mathbf{g} = m_1\mathbf{b}_1 + m_2\mathbf{b}_2 \in \mathbb{R}^2,\ (m_1, m_2) \in \mathbb{Z}^2 \\ 0, & \text{else} \end{array} \right\} \in \mathbb{C}, \tag{11}$$

where $\mathbf{b}_1 \in \mathbb{R}^2$ and $\mathbf{b}_2 \in \mathbb{R}^2$ are the reciprocal primitive vectors. As shown by Eq. (11), the representation of the Gaussian approximated target lattice in the Fourier space is sparse.

Using the rectangular supercell, it is easily shown that for all $\mathbf{g}$ with nonzero $\Psi^{\mathrm{tgt}}(\mathbf{g})$, there exists a corresponding grid point when the Fourier space is appropriately discretized. This indicates that $\Psi^{\mathrm{tgt}}(\mathbf{g})$ remains a sparse representation even after the discretization. The proofs are as follows.

Remark 1. Let $a_{i,j} \in \mathbb{R}$ be the jth component of the primitive vector $\mathbf{a}_i$, where $i \in \{1, 2\}$ and $j \in \{x, y\}$. Without loss of generality, let $a_{1,y} = 0$. When the supercell can be taken as rectangular with a width W and height H, there exists $(m, n, p) \in \mathbb{Z}^3$ such that $W = ma_{1,x}$, $H = na_{2,y}$, and $pa_{1,x} = ma_{2,x}$.

Proof. $W = ma_{1,x}$ and $H = na_{2,y}$ are obvious. The x coordinate of the lattice points at $y = m_2a_{2,y}$ can be written as $m_1a_{1,x} + m_2a_{2,x}$, where $(m_1, m_2) \in \mathbb{Z}^2$. When the supercell can be taken as rectangular, there exists $m_1' \in \mathbb{Z}$ such that $m_1'a_{1,x} = m_1a_{1,x} + m_2a_{2,x}$. Dividing by $a_{1,x}$ on both sides gives $m_2\frac{a_{2,x}}{a_{1,x}} = m_1' - m_1 \in \mathbb{Z}$. Satisfying $m_2\frac{a_{2,x}}{a_{1,x}} \in \mathbb{Z}$ requires that there exists $p \in \mathbb{Z}$ such that $pa_{1,x} = m_2a_{2,x}$. ■

Remark 2. If there exists a rectangular supercell, then rectangular grids can be taken such that for all the reciprocal lattice points, there exists a corresponding grid point.

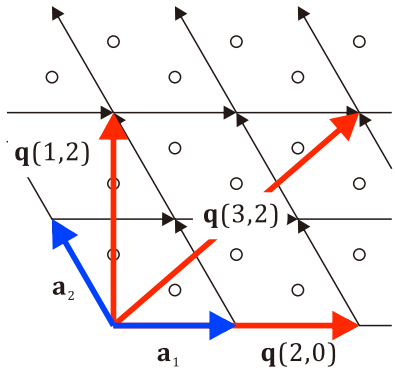

FIG. 3. Schematic illustration of the definition of the rectangular supercell. Primitive vectors are shown as $\mathbf{a}_1$ and $\mathbf{a}_2$. In this figure, $\mathbf{q}(3,2) = \mathbf{q}(2,0) + \mathbf{q}(1,2)$ and $\mathbf{q}(2,0) \cdot \mathbf{q}(1,2) = 0$. Hence, $\mathbf{q}(3,2)$ is an element of $\mathcal{Q}$, which is a set of the candidate vectors pointing along the diagonal of the rectangular supercell. Note that the supercell used in this study is defined by $\mathbf{q}^* = \mathbf{q}(2,2) = \mathbf{q}(1,0) + \mathbf{q}(1,2) \in \mathcal{Q}$, which indicates an upper-right lattice point.

Proof. Let $a_{1,y} = 0$. In this case, $b_{1,x} = 2\pi/a_{1,x}$, $b_{1,y} = -2\pi a_{2,x}/(a_{1,x}a_{2,y})$, $b_{2,x} = 0$, and $b_{2,y} = 2\pi/a_{2,y}$, where $b_{i,j} \in \mathbb{R}$ is the jth component of the reciprocal primitive vector $\mathbf{b}_i$. We define the wave vector at grid point $(p,q) \in \mathbb{Z}^2$ as $(2\pi p/W, 2\pi q/H) := (p\Delta k_x, q\Delta k_y)$. Then, $b_{1,x} = (W/a_{1,x})\Delta k_x$, $b_{1,y} = (-Ha_{2,x}/(a_{1,x}a_{2,y}))\Delta k_y$ and $b_{2,y} = (H/a_{2,y})\Delta k_y$. From Remark 1, there exists $(m,n,p) \in \mathbb{Z}^3$ such that $W = ma_{1,x}$, $H = na_{2,y}$, $pa_{1,x} = na_{2,x}$. Hence, there exists $(m,n,p) \in \mathbb{Z}^3$ such that $b_{1,x} = m\Delta k_x$, $b_{1,y} = -p\Delta k_y$, $b_{2,y} = n\Delta k_y$. This means that when the 2D Fourier space is discretized with spacing $(\Delta k_x, \Delta k_y) = (2\pi/W, 2\pi/H)$, there exists a corresponding grid point for any $\mathbf{b}_i$. ■

To show the sparsity of Ψ^{tgt}, an example of the power spectrum for the honeycomb lattice is presented in Fig. 4. The primitive vectors and atom positions for the honeycomb lattice are illustrated on the left of Fig. 2. As shown in this example, the Fourier representation of the target image is sparse.

The magnitudes of Fourier coefficients of ψ^{tgt} rapidly decrease with an increasing magnitude of the wave vector as shown by Eq. (11) and Fig. 4. Reflecting these properties, only the first M peaks except for the first $k = 0$ peak are considered in this paper. Such an approximation can be seen as low-pass filtering of the Gaussian approximated target lattice. The example of the low-pass filtered image obtained by setting $\psi_{\mathbf{k}_{i>M}} = 0$ is shown on the right of Fig. 2, where $M = 3$. Despite only considering three Fourier coefficients, the positions of atoms of the honeycomb lattice are well represented. Reducing the number of Fourier coefficients of the target lattice decreases the number of trainable parameters. This is because the two-point DCF only appears in the form $C_{2,\mathbf{k}}\psi_{\mathbf{k}}$ as shown on the right-hand side of Eq. (5). That is to say, the trainable parameter can be reduced from $C_{2,k}, k \in \mathbb{R}_+$, to

$$\theta := [C_{2,k_1}\ C_{2,k_2}\ \cdots\ C_{2,k_M}] \in \mathbb{R}^M. \tag{12}$$

In this paper, the number of trainable parameters, M, is treated as a hyperparameter and varies for each desired lattice. In what follows, a set of DCFs, $C_{2,k_1}\ C_{2,k_2}\ \cdots\ C_{2,k_M}$, is referred to as correlation peaks and expressed as $\theta_1, \theta_2, \ldots, \theta_M$.

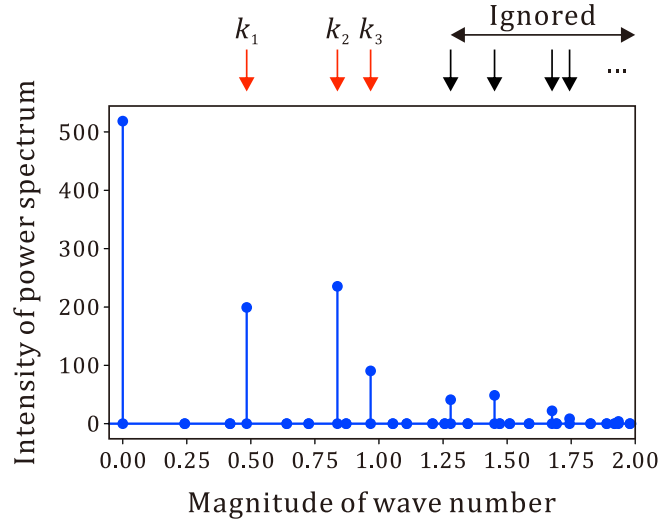

FIG. 4. Example of the Fourier representation of the Gaussian blurred honeycomb lattice. The red arrows indicate the positions of the first three nonzero power spectra except for $k = 0$, where the number three is a hyperparameter. In this case, the trainable parameters are C_{2,k_1}, C_{2,k_2}, and C_{2,k_3}. The target lattice is defined as a Gaussian blurred image whose Fourier coefficient above k_3 is ignored (i.e., $\psi_{>k_3} = 0$).

Treating a small number of correlation peaks suppresses the representation power of the free energy that would provide regularization. This is because a more complicated DCF results in a greater local minimum of the free energy. Restricting the representation power to obtain a better solution is similar to the optimization strategy for the conventional machine learning model [12].

C. Optimization scheme

The gradient descent is used to solve problem Eq. (9) because the gradient of the temporal change in the target free energy with respect to C_2 is easily computed. The loss function $\mathcal{L}(\theta)$ is defined as

$$\mathcal{L}(\theta) = \left| \frac{\partial F[\psi^{\mathrm{tgt}}; \theta]}{\partial t} \right|. \tag{13}$$

The trainable parameter, θ, is updated as

$$\theta \leftarrow \theta - \lambda \frac{\partial \mathcal{L}(\theta)}{\partial \theta}, \tag{14}$$

where λ is the learning rate. One can easily compute the gradient of $\mathcal{L}$ appearing on the right-hand side of Eq. (14) adopting automatic differentiation [13]. Although any type of optimizer can be used, the simplest gradient descent, without using any momentum, is adopted in this paper.

IV. RESULTS AND DISCUSSION

A. Experimental setup

For the target lattices, we used five well-known 2D lattices (i.e., triangular, square, rectangular, honeycomb, and

TABLE I. Primitive vectors and atom coordinates for the target 2D lattices. The space between the closest atoms listed here is normalized to 1. In the experiments, all these values are multiplied by $5\sqrt{3}$. α and β for the ladybug lattice are $\alpha = \sqrt{2+\sqrt{3}}$ and $\beta = \sqrt{2-\sqrt{3}}$.

Lattice	Primitive vectors	Atom coordinates
Triangular	(1,0)	$\left(\frac{1}{4}, \frac{\sqrt{3}}{4}\right)$
	$\left(-\frac{1}{2}, \frac{\sqrt{3}}{2}\right)$	
Square	(1,0)	$\left(\frac{1}{2}, \frac{1}{2}\right)$
	(0,1)	
Rectangular	(1,0)	(0,0)
	(0,4)	(0,2)
Honeycomb	$(\sqrt{3}, 0)$	$\left(\frac{\sqrt{3}}{2}, \frac{1}{2}\right)$
	$\left(-\frac{\sqrt{3}}{2}, \frac{3}{2}\right)$	(0,1)
Kagome	(2,0)	$\left(-\frac{1}{2}, \frac{\sqrt{3}}{2}\right)$
	$(-1, \sqrt{3})$	$\left(\frac{1}{2}, \frac{\sqrt{3}}{2}\right)$
		$(0, \sqrt{3})$
Maple leaf	$(\sqrt{7}, 0)$	$\left(\frac{5\sqrt{7}}{14}, \frac{\sqrt{21}}{14}\right)$
	$\left(-\frac{\sqrt{7}}{2}, \frac{\sqrt{21}}{2}\right)$	$\left(\frac{5\sqrt{7}}{7}, \frac{\sqrt{21}}{7}\right)$
		$\left(\frac{\sqrt{7}}{14}, \frac{3\sqrt{21}}{7}\right)$
		$\left(\frac{3\sqrt{7}}{7}, \frac{2\sqrt{21}}{7}\right)$
		$\left(-\frac{3\sqrt{7}}{14}, \frac{5\sqrt{21}}{14}\right)$
		$\left(\frac{\sqrt{7}}{7}, \frac{3\sqrt{21}}{7}\right)$
Ladybug	$(\alpha, 0)$	$\left(\frac{\alpha-\beta}{4}, \frac{-\alpha-\beta}{4}\right)$
	$(0, \alpha)$	$\left(\frac{-\alpha-\beta}{4}, \frac{-\alpha+\beta}{4}\right)$
		$\left(\frac{-\alpha+\beta}{4}, \frac{\alpha+\beta}{4}\right)$
		$\left(\frac{\alpha+\beta}{4}, \frac{\alpha-\beta}{4}\right)$
Trellis	(1,0)	$\left(\frac{1}{2}, \frac{1}{2}\right)$
	$\left(-\frac{1}{2}, 1+\frac{\sqrt{3}}{2}\right)$	$\left(0, \frac{1}{2}+\frac{\sqrt{3}}{2}\right)$
Lieb	(2,0)	(0,0)
	(0,2)	(1,0)
		(0,1)
CaVO	$(1+\sqrt{2}, 0)$	$\left(\frac{1+\sqrt{2}}{2}, \frac{1}{2}\right)$
	$(0, 1+\sqrt{2})$	$\left(\frac{1}{2}, \frac{1+\sqrt{2}}{2}\right)$
		$\left(\frac{1}{2}+\sqrt{2}, \frac{1+\sqrt{2}}{2}\right)$
		$\left(\frac{1+\sqrt{2}}{2}, \frac{1}{2}+\sqrt{2}\right)$

kagome lattices) and five more 2D lattices (i.e., maple leaf, ladybug, trellis, Lieb, and CaVO lattices). Real materials with more than two types of particle for the maple leaf [14], ladybug [15], Lieb [16], and CaVO [17] lattices have been reported. However, the DCFs for these five lattices have not yet been reported. The primitive vector and the atom coordinates for each lattice are listed in Table I. The hyperparameters used are listed in Table II.

The discretization was carried out as follows. The x and y directions of the ψ^{tgt} in the real space computational region

TABLE II. Hyperparameters used in the optimization.

Description	Symbol	Value
Spacing between nearest atoms	–	$5\sqrt{3}$
Number of correlation peaks	M	Grid search
Coefficient of the Gaussian	α_j	Grid search
Standard deviation of the Gaussian	σ_j	1.5
Mesh spacing	h	0.4
Learning rate	λ	10^{-3}

are divided into N_x and N_y cells, respectively, where

$$N_x = \left\lfloor \frac{W}{h} + 0.5 \right\rfloor, \quad N_y = \left\lfloor \frac{H}{h} + 0.5 \right\rfloor, \tag{15}$$

and h is the mesh spacing. The (p, q) components of the wave vector, $(\mathbf{k})_{pq}$, are then defined as

$$(\mathbf{k})_{pq} = \left(\frac{2\pi p}{W}, \frac{2\pi q}{H} \right), \tag{16}$$

where

$$p \in \left[-\frac{N_x}{2}, \frac{N_x}{2} \right] \subset \mathbb{Z}, \quad q \in \left[-\frac{N_y}{2}, \frac{N_y}{2} \right] \subset \mathbb{Z}. \tag{17}$$

After optimization, PFC simulation using the optimized DCF was carried out. To make it easier to see the periodic pattern, the simulations were carried out in a computational region larger than that used in the optimization. The obtained DCF was mapped to a region five times larger in width and height than the original region. As an example, the computational region is $23\Delta x \times 37\Delta y = a \times \sqrt{3}a$ in the case of the optimization of the triangular lattice and $115\Delta x \times 185\Delta y = 5a \times 5\sqrt{3}a$ in the case of the pattern formation where $\Delta x = W/N_x$ and $\Delta y = H/N_y$. Time integration was carried out using the semi-implicit Fourier spectral method [18] from the initial state sampled from $U([m-\eta, m+\eta]^D)$ until the pattern reached a steady state. The magnitude of the initial noise is taken as $\eta = 0.01$, whereas the mean of the initial condition is the same as the mean of ψ^{tgt}.

In addition to the vanilla PFC simulation with the original optimized DCFs, simulation with the modified DCF was carried out because the original optimized sparse DCFs are not physically valid. Figure 5 shows examples of one-dimensional (1D) plots of the optimized DCF for the CaVO lattice in both Fourier and real spaces. In the case of a sparse DCF, the spatial distribution of the DCF in real space is physically unrealistic [Figs. 5(a) and 5(b)]. A sparse DCF in Fourier space indicates that the interaction force reaches an infinitely distant location without decaying, which is not valid for the physical consideration. In addition, an aliasing problem occurs when the discrete 2D inverse Fourier transformation is applied to the sparse DCF. To address these issues, the optimized DCF is blurred using a Gaussian distribution, which is an approach inspired by [4]

$$\max_m \theta_m \exp\left(-\frac{(k-k_m)^2}{2\bar{\sigma}^2} \right), \tag{18}$$

where $\bar{\sigma}$ is a blurring hyperparameter and $\{k_m, \theta_m\}_{m=1}^M$ is a set of optimized nonzero $C_{2,k}$ and the corresponding k. Blurring the DCF can reduce unrealistic artifacts of its real space

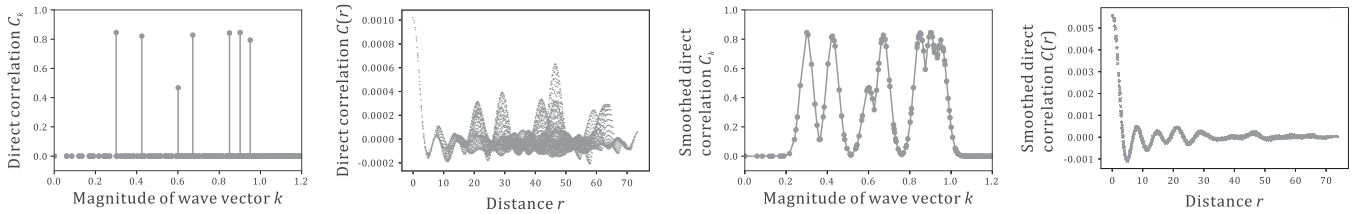

(a) Optimized $C_{2,k}$ (b) Optimized $C_2(r)$ (c) Smoothed $C_{2,k}$ (d) Smoothed $C_2(r)$

FIG. 5. Example of the optimized C_k and the corresponding smoothed version. (a) Optimized C_k for the CaVO lattice. (b) Real–space distribution of C_k for the CaVO lattice. The 1D real–space DCF depicted here is obtained by (i) mapping the 1D C_k to 2D Fourier space, (ii) adopting a discrete 2D inverse Fourier transformation, and (iii) mapping the result to one dimension. (c) Smoothed C_k for (a) obtained using Eq. (18) with $\bar{\sigma} = 0.03$. (d) Real–space distribution of C_k corresponding to (c).

spatial distribution [see Figs. 5(c) and 5(d)] because blurring peaks in Fourier space localizes the corresponding waves in the real space.

We implemented our model with TensorFlow version 1.15.0 [19]. All experiments were carried out on a single NVIDIA P100/V100/GV100 GPU (i.e., one of the GPUs was used).

B. Results

The DCFs obtained adopting the proposed optimization procedure and the corresponding hyperparameters used are listed in Tables III and IV. The numbers of correlation peaks, M, for the triangular, square, rectangular, honeycomb, and kagome lattices are no more than three, which is consistent with the results of a previous study [7], which used a three-mode PFC. Meanwhile, we found that the remaining five lattices (i.e., the maple leaf, ladybug, trellis, Lieb, and CaVO lattices) require at least four correlation peaks. Figures 6 and 7 show temporal changes in the patterns for each lattice obtained using the blurred DCFs with $\bar{\sigma} = 0.03$. The results without DCF blurring are abbreviated because no appreciable difference is observed with and without DCF blurring. As shown in Fig. 6, all five well-known lattices (i.e., triangular, square, rectangular, honeycomb, and kagome lattices) were successfully reproduced (Fig. 7). In addition, the maple leaf, ladybug, trellis, Lieb, and CaVO lattices were successfully reproduced (Fig. 7). The formation of the latter five lattices has been simulated using the PFC model. As mentioned, these lattices require at least four modes and they have thus not been reported.

After optimization, we searched for the minimal number of correlation peaks that represent each lattice as follows. The idea is to remove the correlation peaks contributing less energy from the set of M peaks. The total excess energy defined in Eq. (3) can be broken down to

$$\sum_{i=1}^{M} -\frac{1}{2}\int_{\Omega} \psi(\mathbf{r})\mathcal{F}^{-1}[C_{2,k_i}\psi_{k_i}](\mathbf{r})\mathrm{d}\mathbf{r} := \sum_{i=1}^{M} F_i[\psi], \qquad (19)$$

where $F_i[\psi]$ is the contribution of the ith correlation peak to the total excess energy. This decomposition is inspired

TABLE III. Results of the optimized $C_{2,k}$ for each lattice. The hyperparameters, (M, a_j), determined by conducting a grid search, and the corresponding spatial means of ψ^{tgt}, $\overline{\psi^{\mathrm{tgt}}}$, are also listed.

Lattice	(M, a_j)	$\overline{\psi^{\mathrm{tgt}}}$	(k, C_k)
Triangular	(1,18.0)	0.278 060 54	(0.837 758 02, 0.828 741 35)
Square	(2,18.0)	0.253 297 76	(0.725 519 74, 0.829 614 56), (1.026 039 86, 0.821 743 03)
Rectangle	(3,24.0)	0.169 725 40	(0.362 759 84, 0.843 812 20), (0.725 519 74, 0.863 826 98), (0.811 155 72, 0.844 408 59)
Honeycomb	(3,19.8)	0.215 627 64	(0.483 679 85, 0.838 828 11), (0.837 758 02, 0.837 090 48), (0.967 359 65, 0.817 693 83)
Kagome	(3,19.0)	0.232 780 04	(0.418 878 98, 0.848 152 33), (0.725 519 74, 0.823 694 88), (0.837 758 02, 0.833 521 75)

TABLE IV. *(Continued.)*

Lattice	(M, a_j)	$\overline{\psi^{\mathrm{tgt}}}$	(k, C_k)
maple leaf	(4,18.7)	0.261 801 49	(0.316 642 70, 0.865 382 22), (0.548 441 34, 0.826 682 86), (0.633 285 56, 0.838 602 21), (0.837 758 02, 0.830 371 48)
ladybug	(5,17.5)	0.263 993 48	(0.531 117 31, 0.819 610 60), (0.751 113 31, 0.828 500 98), (0.839 770 21, 0.825 121 89), (1.062 234 63, 0.810 590 92), (1.187 614 42, 0.807 061 13)
trellis	(7,16.0)	0.241 349 64	(0.388 804 84, 0.703 379 36)†, (0.751 113 31, 0.819 899 11), (0.777 609 74, 0.827 470 31), (0.930 864 97, 0.813 210 65), (1.166 414 59, 0.810 038 76)†, (1.212 924 77, 0.801 116 26), (1.451 039 49, 0.777 333 36)
Lieb	(5,19.4)	0.205 776 05	(0.362 759 84, 0.855 960 13), (0.513 019 98, 0.838 192 11), (0.725 519 74, 0.833 889 73), (0.811 155 72, 0.816 962 07), (1.026 039 86, 0.839 413 54)
CaVO	(7,20.6)	0.199 975 51	(0.300 520 05, 0.844 352 21), (0.424 999 65, 0.828 772 59)†, (0.601 040 26, 0.769 595 32)†, (0.671 983 41, 0.841 103 37), (0.849 999 24, 0.845 262 56), (0.901 560 37, 0.842 241 42), (0.950 328 05, 0.785 774 41)†

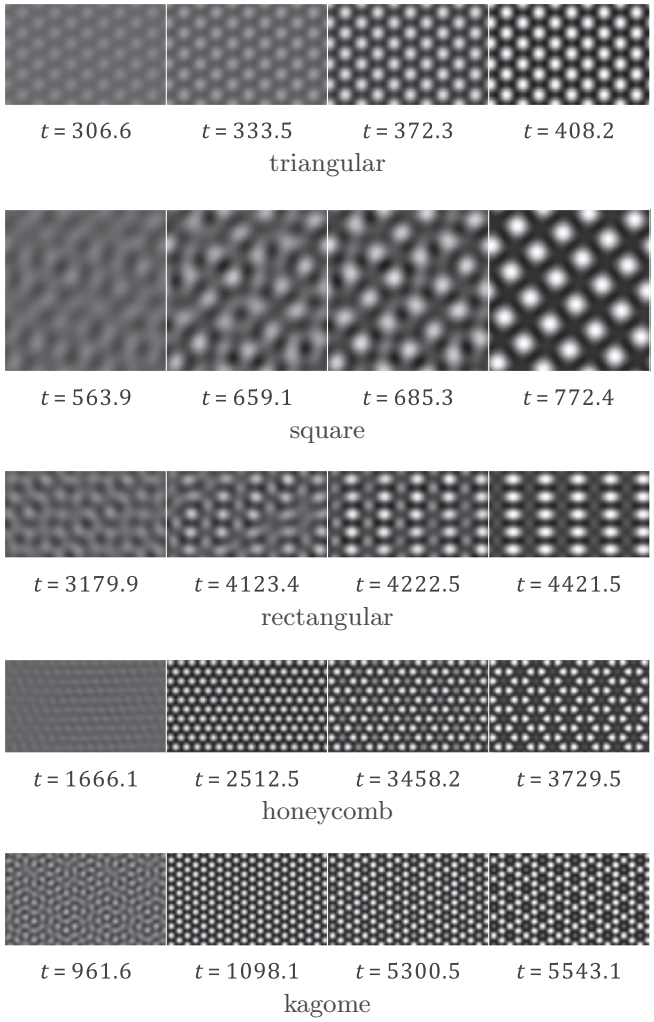

FIG. 6. Snapshots of the pattern formation of the triangular, square, rectangular, honeycomb, and kagome lattices obtained using the optimized DCFs with $\bar{\sigma} = 0.03$ blurring for each lattice.

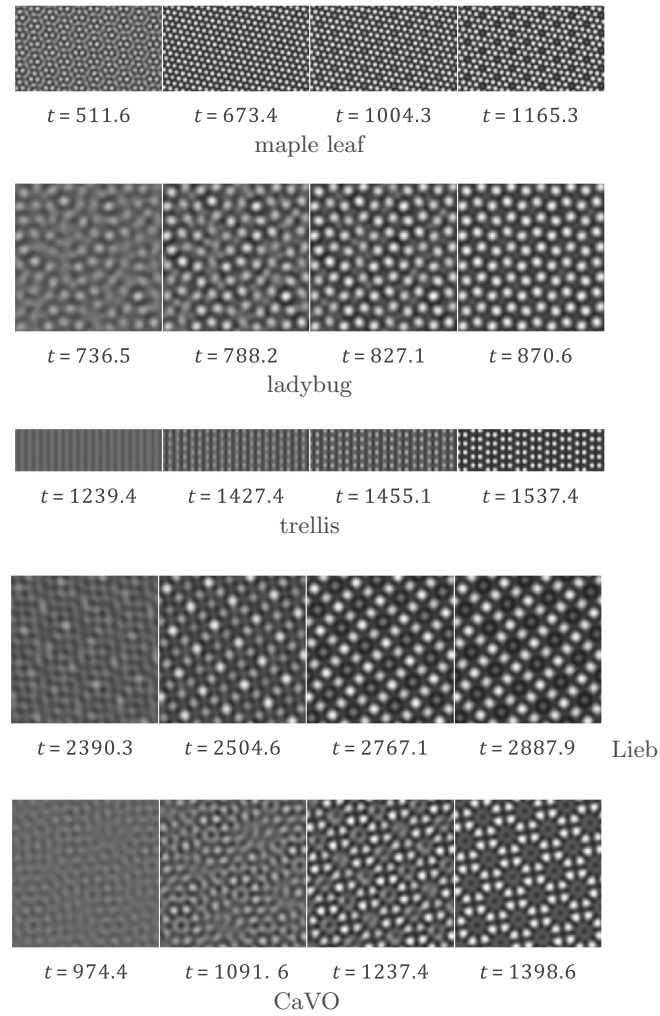

FIG. 7. Snapshots of the pattern formation of the maple leaf, ladybug, trellis, Lieb, and CaVO lattices obtained using the optimized DCFs with $\bar{\sigma} = 0.03$ blurring for each lattice.

by Ref. [5]. We computed $F_i[\psi^{\rm tgt}]$ and removed correlation peaks that contribute less than other peaks to the total excess energy. PFC simulations with the reduced DCFs were then carried out. As a result, the numbers of correlation peaks for the trellis and CaVO lattices were successfully reduced to five and four, respectively. The reduction in the number of correlation peaks failed for the remaining lattices. Total reductions in the excess energy from $F_{\rm excess}[\psi^{\rm tgt}]$ achieved by removing correlation peaks are 1.8% and 9.2% for the trellis and CaVO lattices, respectively. The smallest contributions of $F_i[\psi^{\rm tgt}]$ to the total excess energy for the triangular, square, rectangular, honeycomb, kagome, maple leaf, ladybug, and Lieb lattices are 100%, 23.3%, 24.9%, 7.7%, 10.6%, 4.4%, 3.8%, and 8.3%, respectively. The effect of the peak reduction is small in the case of the trellis lattice compared with that of the failed cases but is somewhat large in the case of the CaVO lattice. To investigate the reason for this, we removed only two of the seven peaks of the CaVO DCF, where these two peaks made the first and second smallest contributions to the total excess energy. PFC simulation was carried out with this five-peaks CaVO DCF. We then computed $F_i[\psi^{\rm gen}]$, where $\psi^{\rm gen}$ is the pattern generated with the five correlation peaks. The result shows that the smallest contribution of $F_i[\psi^{\rm gen}]$ to the total excess energy is 2.4%, which is smaller than that in all the failed cases. In summary, the correlation peaks can be neglected if their contribution to the total excess energy is sufficiently small; i.e., less than about 3%. The patterns obtained using the reduced DCFs for the trellis and CaVO lattices are shown in Fig. 8. We see that the patterns with reduced DCFs are similar to the original patterns depicted on the right of Fig. 7.

V. LIMITATION

Unfortunately, the fully optimized DCFs do not always generate the desired pattern for some lattices. Figure 9 shows competitive patterns generated using a specific initial condition for the maple leaf, ladybug, Lieb, and CaVO lattices. Among these competitive patterns, we found that some are energetically indistinguishable from the desired lattice. Figure 10 compares $F_i[\psi^{\rm gen}]$ between the generated CaVO pattern and its competitive patterns, where comp. represents

FIG. 8. Patterns generated with reduced DCFs. There are five and four correlation peaks for the trellis and CaVO lattices, respectively. The removed correlation peaks are indicated in Table III with superscript daggers.

the competitive pattern. The difference in excess energy between CaVO and comp. 2 is clear whereas $F_i[\psi^{\rm gen}]$ for CaVO and comp. 1 are almost the same for all peaks. This suggests that CaVO and comp 2 are visibly different but hard to distinguish from the viewpoint of the energy landscape. The pattern formation is governed by the free energy in the PFC, and the current simplified free–energy Eq. (1), which includes assumptions (i)–(iv) described in Sec. II, should thus be modified to avoid energetically similar competitive patterns such as comp. 1. In Appendix A 1, we tried to find a liquid-CaVO coexisting region adopting an analytic approach, which obtains the phase diagram using approximated target patterns, but it is difficult to determine such a region because the calculated phase diagram has $M+1$ dimensions. In addition, such a liquid-target phase coexisting region may be narrow [see Fig. 12(e)], which suggests that a highly accurate approximation for the target phase that actually appeared as the stable solution of the PFC equation is required. The effects of higher-order DCFs on suppressing the competitive patterns are discussed in Appendix B. Note that for the other lattices (i.e., the triangular, square, rectangular, honeycomb, kagome, and trellis lattices), competitive patterns were not observed in the present experiments.

Another remaining problem is the difficulty of the polycrystallization simulation. As discussed above, there are competitive patterns that are energetically more stable than the target pattern. This makes the polycrystallization simulation difficult because the competitive patterns more likely form during the crystallization. Figures 11(a) and 11(b) show the

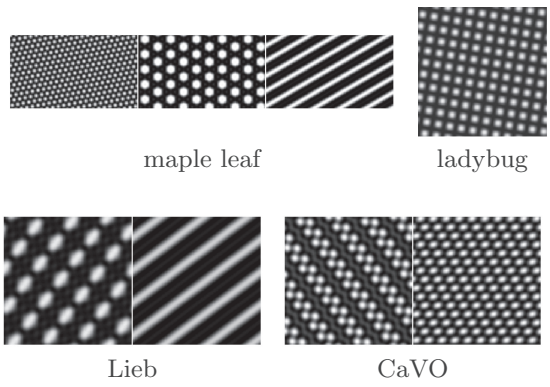

FIG. 9. Competitive patterns for each lattice. The name of the desired lattice is given below the patterns. No competitive patterns were found for the other lattices in the experiments.

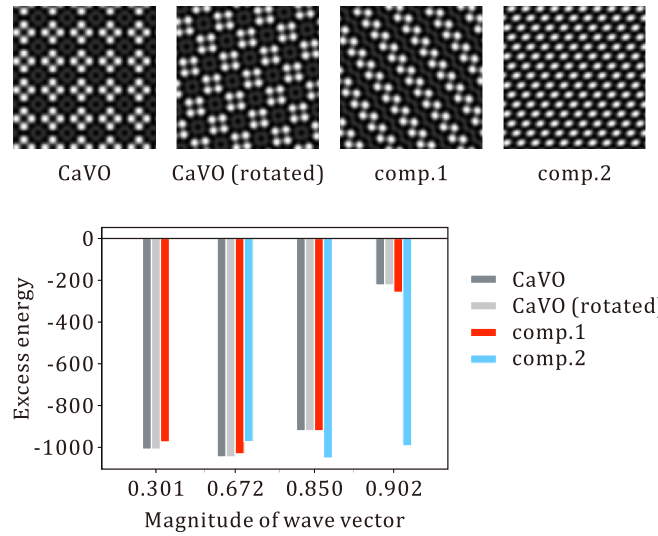

FIG. 10. Comparison of excess energy between the generated CaVO and competitive patterns. Two desired patterns, the CaVO and CaVO (rotated) patterns, are depicted above because the desired CaVO patterns can be rotated whenever the periodic boundary condition is satisfied. Comp. 1 and comp. 2 are competitive patterns that are different from the desired pattern. All patterns are generated with the reduced DCF.

results of the polycrystallization simulation with the two point nuclei in the case of the CaVO lattice. When $\sigma = 0$, the single crystal of the CaVO lattice is generated but the crystallization process is physically unnatural because the correlation force reaches infinitely distant space and the crystallization occurs simultaneously throughout the calculation region. Meanwhile, in the case of $\sigma = 0.3$, the crystallization gradually occurs from the nuclei. However, although the CaVO motif defined in Fig. 11(a) appears locally in Fig. 11(b), the generated lattice does not match the CaVO pattern.

Figure 11(c) shows the crystal growth from the existing two CaVO crystals. The CaVO pattern gradually develops from the initial crystals and a disturbed structure is seen between the crystals. This disturbed structure may be referred to as crystal defects but one should carefully interpret the physical meaning of this structure because the present simulation has the aforementioned problems.

VI. RELATED WORKS

The works most related to the present paper investigated an inverse design of a pair potential in a particle system. Pair potentials with a single type of particle for square [20–23], rectangular [21], honeycomb [21–23], kagome [21–24], snub square (ladybug) [24], truncated square (CaVO) [21,22,25], truncated hexagonal [21,22,25,26], and trihexagonal [26] lattices have been reported whereas more complex structures have been successfully reproduced by allowing particle selectivity [27] or using more than two types of particle [28–30]. Although the pair potential is strongly correlated to the two-point DCF as mentioned below, obtaining the two-point DCF from the pair potential is intractable.

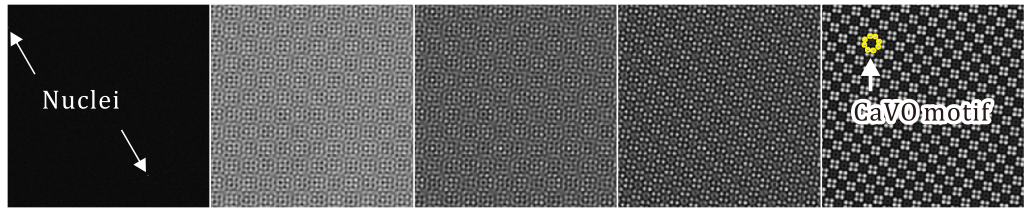

$t = 0$ $t = 762$ $t = 3{,}141$ $t = 3{,}250$ $t = 3{,}997$

(a) $\sigma = 0$ with point nuclei

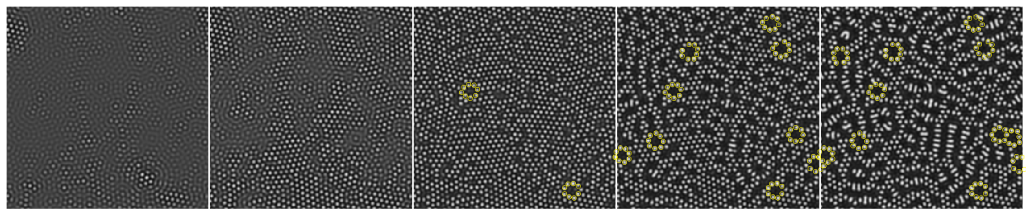

$t = 2{,}299$ $t = 2{,}395$ $t = 2{,}603$ $t = 3{,}433$ $t = 6{,}705$

(b) $\sigma = 0.3$ with point nuclei

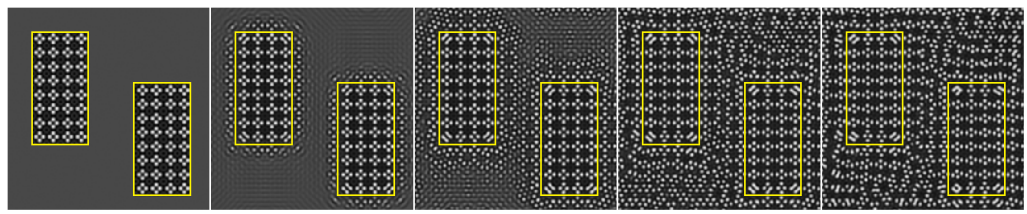

$t = 0$ $t = 166$ $t = 353$ $t = 902$ $t = 2{,}188$

(c) $\sigma = 0.3$ with structured nuclei

FIG. 11. Results of the CaVO crystallization simulations: (a) $\sigma = 0$ with two point nuclei, (b) $\sigma = 0.3$ with the same initial conditions as (a), (c) $\sigma = 0.3$ with crystalline nuclei. The crystalline nucleus is obtained by repeatedly arranging Fig. 8 (right) horizontally and vertically. The yellow circles in (b) indicate the CaVO motif as illustrated in (a). The yellow rectangles in (c) are the initial boundaries of the crystalline nuclei.

There are two existing approaches that can be adopted to obtain the DCF. One is solving the Ornstein–Zernike (OZ) equation and the closure [31] simultaneously using a given potential. However, in general, an approximation is required for the bridge function appearing in the closure because the concrete representation of the bridge function is not known. The molecular dynamics simulation approach is an alternative to obtain the DCF. Instead of using the closure, a molecular dynamic simulation is carried out using a given potential. An n-particle density and a pair correlation function are calculated in subsequent post-processing. The DCF is then computed by solving the OZ equation. Note that in the case of isotropic liquids, the OZ equation can be reduced to the 1D equation whereas it cannot in the case of a crystal. This is because the pair correlation depends not only on the distance but also the angle in the case of a crystal. This complicates the solving of the OZ equation.

Compared with the existing methods, our approach is straightforward in obtaining the DCF. Our ultimate goal is not to obtain the potential but to get the DCF because the latter is required for PFC simulation. This is the main difference between the existing method and our approach.

In this paper, the DCFs are decomposed into each separated modes, which is similar to the concept of an amplitude equation [32–37]. In the amplitude equation, the time development of the amplitude of each mode is calculated and the original phase is then reconstructed using these amplitudes. The difference is that the proposed model simply decomposes the two-point DCF into each mode and does not decompose the amplitudes.

VII. CONCLUSIONS

We proposed an optimization method to obtain a two-point DCF, C_2, corresponding to a desired lattice. Using the present method, we found C_2 not only for five well-known lattices (i.e., triangular, square, rectangular, honeycomb, and kagome lattices) but also for five nontrivial lattices (i.e., maple leaf, ladybug, trellis, Lieb, and CaVO lattices). In addition, we showed that these lattices can be simulated with a five-mode PFC. The open question is how to stabilize these patterns and what type of crystal defects can be generated. We hope that the present paper will accelerate a wide range of applications of the PFC.

TABLE V. Parameters for the lattices appearing in the CaVO system. In all phases, $(L_x, L_y) = (a^{\rm st}_{1,x}, a^{\rm st}_{2,y})$.

Phase	$\mathbf{r}_j$	$\mathcal{K}_m$
CaVO	$\mathbf{r}_1 = \frac{1}{2}\mathbf{a}^{\rm st}_1 + \frac{\sqrt{2}-1}{2}\mathbf{a}^{\rm st}_2$	$\mathcal{K}_1 = \{(\Delta k_x, -\gamma_{xy}\Delta k_x), (0, \Delta k_y)\}$
(sine terms cancel out)	$\mathbf{r}_2 = \frac{\sqrt{2}-1}{2}\mathbf{a}^{\rm st}_1 + \frac{1}{2}\mathbf{a}^{\rm st}_2$	$\mathcal{K}_4 = \{(\Delta k_x, 2\Delta k_y - \gamma_{xy}\Delta k_x), (2\Delta k_x, \Delta k_y - 2\gamma_{xy}\Delta k_x, \Delta k_y),$ $(-\Delta k_x, 2\Delta k_y + \gamma_{xy}\Delta k_x), (-2\Delta k_x, \Delta k_y + 2\gamma_{xy}\Delta k_x, \Delta k_y)\}$
	$\mathbf{r}_3 = \frac{3-\sqrt{2}}{2}\mathbf{a}^{\rm st}_1 + \frac{1}{2}\mathbf{a}^{\rm st}_2$	$\mathcal{K}_5 = \{(2\Delta k_x, 2\Delta k_y - 2\gamma_{xy}\Delta k_x), (-2\Delta k_x, 2\Delta k_y + 2\gamma_{xy}\Delta k_x)\}$
	$\mathbf{r}_4 = \frac{1}{2}\mathbf{a}^{\rm st}_1 + \frac{3-\sqrt{2}}{2}\mathbf{a}^{\rm st}_2$	$\mathcal{K}_6 = \{(3\Delta k_x, -3\gamma_{xy}\Delta k_x), (0, 3\Delta k_y)\}$
Zigzag	$\mathbf{r}_1 = \frac{1}{2}\mathbf{a}^{\rm st}_1 + \frac{1}{4}\mathbf{a}^{\rm st}_2$	$\mathcal{K}_1 = \{(\Delta k_x, -\gamma_{xy}\Delta k_x)\}$
	$\mathbf{r}_2 = \frac{1}{2}\mathbf{a}^{\rm st}_1 + \frac{3}{4}\mathbf{a}^{\rm st}_2$	$\mathcal{K}_4 = \{(\Delta k_x, 2\Delta k_y - \gamma_{xy}\Delta k_x), (-\Delta k_x, 2\Delta k_y + \gamma_{xy}\Delta k_x)\}$
	$\mathbf{r}_3 = \frac{3-\sqrt{2}}{2}\mathbf{a}^{\rm st}_1$	$\mathcal{K}_5 = \{(2\Delta k_x, 2\Delta k_y - 2\gamma_{xy}\Delta k_x), (-2\Delta k_x, 2\Delta k_y + 2\gamma_{xy}\Delta k_x)\}$
	$\mathbf{r}_4 = \frac{3-\sqrt{2}}{2}\mathbf{a}^{\rm st}_1 + \frac{1}{2}\mathbf{a}^{\rm st}_2$	$\mathcal{K}_6 = \{(3\Delta k_x, -3\gamma_{xy}\Delta k_x)\}$
Oblique	$\mathbf{r}_1 = \frac{1}{6}\mathbf{a}^{\rm st}_1 + \frac{5}{12}\mathbf{a}^{\rm st}_2$	$\mathcal{K}_4 = \{(\Delta k_x, 2\Delta k_y - \gamma_{xy}\Delta k_x)\}$
(sine terms cancel out)	$\mathbf{r}_2 = \frac{1}{6}\mathbf{a}^{\rm st}_1 + \frac{11}{12}\mathbf{a}^{\rm st}_2$	$\mathcal{K}_5 = \{(-2\Delta k_x, 2\Delta k_y + 2\gamma_{xy}\Delta k_x)\}$
	$\mathbf{r}_3 = \frac{1}{2}\mathbf{a}^{\rm st}_1 + \frac{1}{4}\mathbf{a}^{\rm st}_2$	$\mathcal{K}_6 = \{(3\Delta k_x, -3\gamma_{xy}\Delta k_x)\}$
	$\mathbf{r}_4 = \frac{1}{2}\mathbf{a}^{\rm st}_1 + \frac{3}{4}\mathbf{a}^{\rm st}_2$	
	$\mathbf{r}_5 = \frac{5}{6}\mathbf{a}^{\rm st}_1 + \frac{1}{12}\mathbf{a}^{\rm st}_2$	
	$\mathbf{r}_6 = \frac{5}{6}\mathbf{a}^{\rm st}_1 + \frac{7}{12}\mathbf{a}^{\rm st}_2$	
Stripe (sine terms cancel out)	$\mathbf{r}_1 =$ arbitrary	$\mathcal{K}_6 = \{(3\Delta k_x, -3\gamma_{xy}\Delta k_x)\}$

APPENDIX A: ANALYSIS OF FREE ENERGY

In this Appendix, we discuss the phase diagram and the elasticity induced by the present form of the free-energy functional. The procedure to obtain the phase diagram and the elastic constants is the same as that reported in the literature [2].

Without loss of generality, the ordered patterns are approximately represented as

$$\psi(\mathbf{r}; a, A, \bar{\psi}, \boldsymbol{\epsilon}) = \bar{\psi} + a\sum_{m=1}^{M}\sum_{\mathbf{k}\in\mathcal{K}_m(A,\boldsymbol{\epsilon})}\psi_m(\mathbf{r}; \mathbf{k}, A, \boldsymbol{\epsilon}), \quad \text{(A1)}$$

where

$$\psi_m(\mathbf{r}; \mathbf{k}, A, \boldsymbol{\epsilon}) = \sum_{j=1}^{N_{\rm atoms}}[\cos(\mathbf{k}\cdot\mathbf{r}_j(A,\boldsymbol{\epsilon}))\cos(\mathbf{k}\cdot\mathbf{r}) + \sin(\mathbf{k}\cdot\mathbf{r}_j(A,\boldsymbol{\epsilon}))\sin(\mathbf{k}\cdot\mathbf{r})]. \quad \text{(A2)}$$

Here, $\mathbf{r}$ denotes the coordinates, a the amplitude, A the distance between the nearest-neighboring atoms, and $\bar{\psi}$ the spatial mean of ψ. $\boldsymbol{\epsilon} = (\epsilon_x, \epsilon_y, \gamma_{xy})$, where ϵ_x, ϵ_y, and γ_{xy} are the normal strain along the x axis, the normal strain along the y axis, and the shear strain along the x axis on the y plane, respectively. $\mathbf{r}_j$ denotes the jth atom coordinates and $\mathcal{K}_m$ the set of wave vectors corresponding to the mth correlation peak. Note that $\forall\mathbf{k}\in\mathcal{K}_m(A,\mathbf{0})$, $|\mathbf{k}| = k_m$. Using this representation and the smoothed version of C_2 defined in Eq. (18), the term $\int_\Omega C_2(|\mathbf{r}-\mathbf{r}'|)\psi(\mathbf{r}')d\mathbf{r}'$ appearing in the present free-energy functional is calculated as

$$\int_\Omega C_2(|\mathbf{r}-\mathbf{r}'|)\psi(\mathbf{r}')d\mathbf{r}' = a\sum_{m=1}^{M}\theta_m\sum_{\mathbf{k}\in\mathcal{K}_m(A,\boldsymbol{\epsilon})}e^{-\frac{(|\mathbf{k}|-k_m)^2}{2\bar{\sigma}^2}}\psi_m(\mathbf{r}; \mathbf{k}, A, \boldsymbol{\epsilon}). \quad \text{(A3)}$$

Note that this expression is only valid in the limit of small $\bar{\sigma}$ that satisfies $C_{\mathbf{k}} \approx \sum_{m=1}^{M}\theta_m\exp(-(|\mathbf{k}|-k_m)^2/(2\bar{\sigma}^2))$. The unit cell region is written as

$$\Omega(A, \boldsymbol{\epsilon}) = [0, L_x(A, \boldsymbol{\epsilon})] \times [0, L_y(A, \boldsymbol{\epsilon})], \quad \text{(A4)}$$

where $L_x(A, \boldsymbol{\epsilon})$ and $L_y(A, \boldsymbol{\epsilon})$ are, respectively, the width and height of the strained unit cell. The strained primitive vectors are

$$\mathbf{a}^{\rm st}_i(A, \boldsymbol{\epsilon}) = \begin{bmatrix}(1+\epsilon_x)a_{i,x} + \gamma_{xy}(1+\epsilon_y)a_{i,y}\\ (1+\epsilon_y)a_{i,y}\end{bmatrix} \quad \text{(A5)}$$

for $i = 1, 2$.

In the case of the triangular lattice, sine terms in Eq. (A2) cancel out owing to the geometric symmetry, $N = M = 1$, $L_x(A, \boldsymbol{\epsilon}) = a^{\rm st}_{1,x}(A, \boldsymbol{\epsilon})$, $L_y(A, \boldsymbol{\epsilon}) = 2a^{\rm st}_{2,y}(A, \boldsymbol{\epsilon})$, $\mathbf{r}_1 = (\mathbf{a}^{\rm st}_1(A, \boldsymbol{\epsilon}) + \mathbf{a}^{\rm st}_2(A, \boldsymbol{\epsilon}))/2$, $\mathcal{K}_1(A, \boldsymbol{\epsilon}) = \{[0 \quad 2\Delta k_y(A, \boldsymbol{\epsilon})]^{\mathsf{T}}, [\Delta k_x(A, \boldsymbol{\epsilon}) \quad \Delta k_y(A, \boldsymbol{\epsilon}) - \gamma_{xy}\Delta k_x(A, \boldsymbol{\epsilon})]^{\mathsf{T}}$, and $[-\Delta k_x(A, \boldsymbol{\epsilon}) \quad \Delta k_y(A, \boldsymbol{\epsilon}) + \gamma_{xy}\Delta k_x(A, \boldsymbol{\epsilon})]^{\mathsf{T}}$, where $\Delta k_x(A, \boldsymbol{\epsilon}) = 2\pi/L_x(A, \boldsymbol{\epsilon})$ and $\Delta k_y(A, \boldsymbol{\epsilon}) = 2\pi/L_y(A, \boldsymbol{\epsilon})$. We calculated the corresponding parameters for the CaVO system and summarize them in Table V.

1. Phase diagram

Solving

$$a^*(\bar{\psi}, \theta_1), A^*(\bar{\psi}, \theta_1) = \underset{a,A}{\rm argmin}\frac{F[\psi(\mathbf{r}; a, A, \bar{\psi}, \mathbf{0}); \theta_1]}{|\Omega(A, \mathbf{0})|}$$

with Mathematica version 11.3 [38], we obtain $a^*(\bar{\psi}, \theta_1) = (1 - 2\bar{\psi} + \sqrt{-19 + 20\theta_1 + 16\bar{\psi}(1-\bar{\psi})})/5$ for $\bar{\psi} \leqslant \frac{1}{2}$, $a^*(\bar{\psi}, \theta_1) = (1 - 2\bar{\psi} - \sqrt{-19 + 20\theta_1 + 16\bar{\psi}(1-\bar{\psi})})/5$ for $\bar{\psi} > \frac{1}{2}$. $A^*(\bar{\psi}, \theta_1)$ is arbitrary because F/Ω does not depend on A.

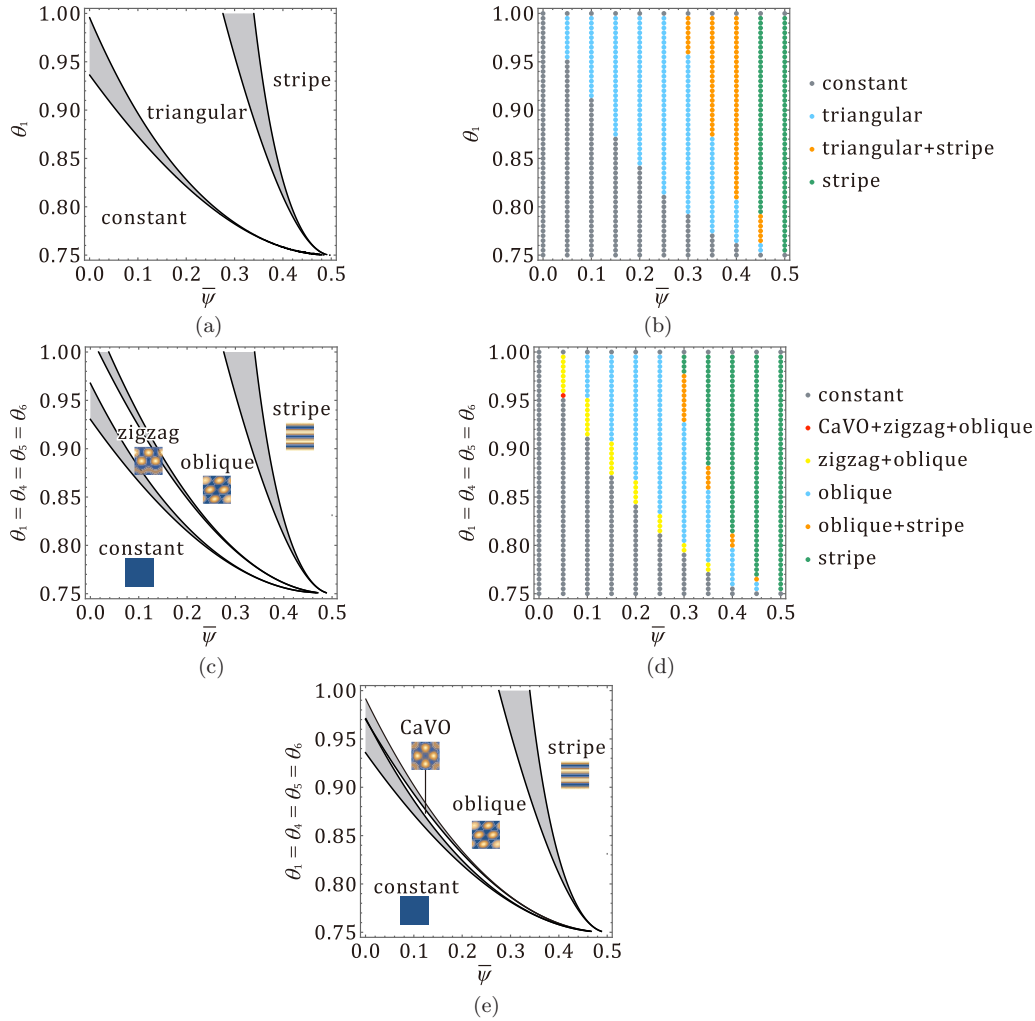

FIG. 12. (a) Analytically obtained phase diagram of the triangular system, (b) simulation results of the triangular system, (c) analytically obtained phase diagram of the CaVO system, (d) simulation results of the CaVO system, and (e) analytically obtained phase diagram of the CaVO system excluding the zigzag phase. Gray regions in (a), (c), and (e) are the coexisting regions of neighboring phases.

In the case of the triangular lattice, the stripe pattern appears as a competitive pattern. The stripe pattern is expressed as $\psi(\mathbf{r}; a, A, \bar{\psi}, \boldsymbol{\epsilon}) = \bar{\psi} + a\alpha_1(\mathbf{k}, A, \boldsymbol{\epsilon})\cos(\mathbf{k}\cdot\mathbf{r})$, where $\mathbf{k} \in \mathcal{K}_1(A, \boldsymbol{\epsilon})$. The difference between the triangular and stripe lattices is that the number of $\mathbf{k} \in \mathcal{K}_1$ considered. All $\mathbf{k} \in \mathcal{K}_1$ are considered in the case of the triangular lattice whereas only one of $\mathbf{k} \in \mathcal{K}_1$ is considered in the case of the stripe lattice.

The region of liquid–solid coexistence can be determined using the so-called tangent rule as $[\psi_1, \psi_2]$ where ψ_1 and ψ_2 are the solutions to the equations

$$\left.\begin{aligned} f_\ell(\psi_1) - \psi_1 \frac{\partial f_\ell}{\partial \psi}(\psi_1) &= f_c(\psi_2) - \psi_2 \frac{\partial f_c}{\partial \psi}(\psi_2) \\ \frac{\partial f_\ell}{\partial \psi}(\psi_1) &= \frac{\partial f_c}{\partial \psi}(\psi_2), \end{aligned}\right\} \tag{A6}$$

where

$$\begin{aligned} f_\ell(\psi) &:= \frac{F[\psi(\mathbf{r}; 0, A^*, \bar{\psi}, \mathbf{0}); \boldsymbol{\theta}]}{|\Omega(A^*, \mathbf{0})|}, \\ f_c(\psi) &:= \frac{F[\psi(\mathbf{r}; a^*, A^*, \bar{\psi}, \mathbf{0}); \boldsymbol{\theta}]}{|\Omega(A^*, \mathbf{0})|} (a^* \neq 0). \end{aligned} \tag{A7}$$

The triangular-stripe coexistence region can be obtained in the same way described above. The resulting phase diagram is illustrated as Fig. 12(a). This phase diagram is qualitatively in good agreement with the existing result [2]. Numerical simulations with varying $\bar{\psi}$ and θ_1 were carried out for the verification of the present analysis. For the entire set of $(\bar{\psi}, \theta_1)$, the PFC equation is calculated for the 16 initial conditions until the pattern reaches the steady state. The obtained patterns are then recorded. The result shown in Fig. 12(b) is very consistent with Fig. 12(a).

In the same way, the optimal amplitude of the four-peaks CaVO is obtained as $a^*_{\text{cavo}}(\bar{\psi}, \theta_1, \theta_4, \theta_5, \theta_6) = 0.036 - 0.072\bar{\psi} + 0.053\sqrt{-7.712 + \Theta + 6.313\bar{\psi}(1-\bar{\psi})}$ for $\bar{\psi} \leqslant 1/2$, $a^*_{\text{cavo}}(\bar{\psi}, \theta_1, \theta_4, \theta_5, \theta_6) = 0.036 - 0.072\bar{\psi} - 0.053\sqrt{-7.712 + \Theta + 6.313\bar{\psi}(1-\bar{\psi})}$ for $\bar{\psi} > 1/2$ where $\Theta := 0.490\theta_1 + 2.302\theta_4 + 2.682\theta_5 + 2.704\theta_6$ and $A^*(\bar{\psi}, \theta_1)$ is arbitrary because F/Ω does not depend on A. Although we obtained the analytic results of a^*, we only present the numerically evaluated results owing to space limitations.

Analytically and numerically obtained phase diagrams of the CaVO lattices are depicted in Figs. 12(c) and 12(d),

respectively. Here, we assumed $\theta_1 = \theta_4 = \theta_5 = \theta_6$ for the 2D visualization. The figure shows that the region of the stripe and oblique phases are in good agreement but the CaVO phase only appears in the numerical results. In the analytic phase diagram, although the energy difference is very small, the zigzag phase, which is the same as comp. 1 in Fig. 10, has lower energy than the CaVO phase. The difference between these diagrams is due to the approximation of the ordered patterns described by Eq. (A1). For instance, a parameter σ in Eq. (10) that controls the spatial size of the high–density region is not considered for simplicity.

If the zigzag phase is successfully removed from Fig. 12(c), Fig. 12(e) is obtained. This phase diagram is calculated without considering the zigzag phase. The figure shows that there exists a constant(liquid)-CaVO coexistence region. In other words, to obtain the stable CaVO phase, suppressing the zigzag phase by increasing the zigzag energy or by decreasing the CaVO energy is essential.

2. Elasticity

Independent components of the elastic constants in the case of 2D lattices are $C_{11}, C_{22}, C_{66}, C_{12}, C_{16}$, and C_{26} where C_{ij} is the component of the elastic coefficient matrix in the Voigt notation. For generality, we did not assume any symmetry (e.g., cubic symmetry) of the lattice. Following Ref. [2], the elastic constants are calculated as

$$\begin{aligned} C_{11} &= \mathcal{C}(\mathcal{G}(\epsilon, 0, 0), \epsilon^2), \\ C_{22} &= \mathcal{C}(\mathcal{G}(0, \epsilon, 0), \epsilon^2), \\ C_{66} &= \mathcal{C}(\mathcal{G}(0, 0, \epsilon), \epsilon^2), \\ C_{12} &= \mathcal{C}(\mathcal{G}(\epsilon, \epsilon, 0), \epsilon^2) - (C_{11} + C_{22})/2, \\ C_{16} &= \mathcal{C}(\mathcal{G}(\epsilon, 0, \epsilon), \epsilon^2) - (C_{11} + C_{66})/2, \\ C_{26} &= \mathcal{C}(\mathcal{G}(0, \epsilon, \epsilon), \epsilon^2) - (C_{22} + C_{66})/2, \end{aligned} \tag{A8}$$

where

$$\mathcal{G}(\epsilon_x, \epsilon_y, \gamma_{xy}) = \frac{F[\psi(\mathbf{r}; a^*, A^*, \bar{\psi}, \epsilon_x, \epsilon_y, \gamma_{xy}); \theta_1]}{|\Omega(A, (\epsilon_x, \epsilon_y, \gamma_{xy}))|} \tag{A9}$$

and $\mathcal{C}(\text{expr}, x)$ indicates the coefficient of x in expr. Note that F_{ideal} does not contribute to the elasticity because it does not include spatial gradient terms of ψ. The term F_{ideal} can thus be ignored in the calculation of the elastic constants. The resulting elastic constants for the triangular lattice are

$$\frac{C_{11}}{3} = \frac{C_{22}}{3} = C_{12} = C_{66} = \frac{\pi^2 a^{*2} \theta_1}{2A^{*2}\bar{\sigma}^2}$$

and

$$C_{16} = C_{26} = 0.$$

In the same way, the elastic constants for the square, honeycomb, and kagome lattices were calculated. The results are

$$\begin{aligned} \frac{\theta_2}{\theta_1 + \theta_2} C_{11} = \frac{\theta_2}{\theta_1 + \theta_2} C_{22} = C_{66} = C_{12} &= \frac{\pi^2 a_{\text{sq}}^{*2} \theta_2}{A^{*2}\bar{\sigma}^2}, \\ \frac{C_{11}}{3} = \frac{C_{22}}{3} = C_{66} = C_{12} &= \frac{\pi^2 a_{\text{hon}}^{*2} (\theta_1 + 12\theta_2 + 4\theta_3)}{6A^{*2}\bar{\sigma}^2}, \\ \frac{C_{11}}{3} = \frac{C_{22}}{3} = C_{66} = C_{12} &= \frac{\pi^2 a_{\text{kag}}^{*2} (\theta_1 + 3\theta_2 + 36\theta_3)}{8A^{*2}\bar{\sigma}^2}, \end{aligned}$$

respectively, where $a_{\text{sq}}^* = [1 - 2\bar{\psi} + (-17 + 9\theta_1 + 9\theta_2 + 14\bar{\psi}(1 - \bar{\psi}))^{1/2}]/9$, $a_{\text{hon}}^* = [15 - 30\bar{\psi} + (-3063 + 548\theta_1 + 2192\theta_2 + 548\theta_3 + 2388\bar{\psi}(1 - \bar{\psi}))^{1/2}]/137$ and $a_{\text{kag}}^* = [178 - 356\bar{\psi} + 2(-136817 + 13158\theta_1 + 13158\theta_2 + 118422\theta_3 + 113054\bar{\psi}(1 - \bar{\psi}))^{1/2}]/2193$ for $\bar{\psi} \leqslant 1/2$. The elastic constants for the four-peaks CaVO can be calculated in the same way. The results are

$$\begin{aligned} C_{11} = C_{22} = \frac{16(3 - 2\sqrt{2})\pi^2 a_{\text{cavo}}^{*2}}{5A^{*2}\bar{\sigma}^2} &\left(5\cos^4\left(\frac{\pi}{\sqrt{2}}\right)\theta_1 \right. \\ &+ 34(1 - 2\cos(\sqrt{2}\pi))^2 \cos^4\left(\frac{\pi}{\sqrt{2}}\right)\theta_4 \\ &\left. + 20\cos^2(2\sqrt{2}\pi)\theta_5 + 45\cos^4\left(\frac{3\pi}{\sqrt{2}}\right)\theta_6 \right) \\ C_{66} = C_{12} = \frac{32(3 - 2\sqrt{2})\pi^2 a_{\text{cavo}}^{*2}}{5A^{*2}\bar{\sigma}^2} &\\ \times \left(8\cos^4\left(\frac{\pi}{\sqrt{2}}\right)\theta_4 + 10\cos^2(2\sqrt{2}\pi)\theta_5 \right) &\\ C_{16} = C_{26} = 0. & \end{aligned}$$

From these results, we obtain the relationships $C_{22} = C_{11}$ and $C_{16} = C_{26} = 0$ for all the above lattices and $2C_{66} = C_{11} - C_{12}$ for the triangular, honeycomb, and kagome lattices, which are consistent with the relationships of the second-order elastic constants [39]. In addition, we find that blurring the DCF is essential to obtaining the finite elastic constants because $C_{ij} \to \infty$ when $\bar{\sigma} \to 0$.

APPENDIX B: EFFECT OF NONLINEARITY

To discuss the effect of the nonlinearity of ψ in the free–energy functional, assumptions (ii) and (iv) described in Sec. II are modified. First, the DCFs higher than third order are approximated as $C_k \approx c_0^{(k)} \prod_{i=2}^{k} \delta(\mathbf{r} - \mathbf{r}_i)$, which is known as the local density approximation [11]. Second, $O(\psi^{N+1})$ terms is ignored. Under these approximations, the free–energy functional is written as

$$F[\psi] = \int \mathrm{d}\mathbf{r} \sum_{k=3}^{N} \left(\frac{(-1)^{k+1}}{k} + \frac{(-1)^k}{k-1} - \tilde{c}^{(k)} \right) \psi^k(\mathbf{r}) + g(\psi). \tag{B1}$$

Here, $\tilde{c}^{(k)} = \rho_0 c_0^{(k)}/(k-1)!$, where ρ_0 is the reference density, and $g(\psi) = \psi(\mathbf{r})(\psi(\mathbf{r}) - \int \mathrm{d}\mathbf{r}' C_2(|\mathbf{r} - \mathbf{r}'|)\psi(\mathbf{r}'))/2$. Following Ref. [40], $\psi(\mathbf{r}) = \bar{\psi} + \sum_{\mathbf{q}\neq\mathbf{0}} a_{\mathbf{q}} e^{i\mathbf{q}\cdot\mathbf{r} + \phi_{\mathbf{q}}}$ is substituted into Eq. (B1), giving

$$\begin{aligned} &F\left[\bar{\psi} + \sum_{\mathbf{q}\neq\mathbf{0}} a_{\mathbf{q}} e^{i\mathbf{q}\cdot\mathbf{r} + \phi_{\mathbf{q}}} \right] \\ &\quad = F[\bar{\psi}] + G + \sum_{j=3}^{N} \alpha_j \sum_{\mathbf{q}_1, \ldots, \mathbf{q}_j} \beta_{\mathbf{q}_1, \ldots, \mathbf{q}_j} \delta(\mathbf{q}_1 + \cdots + \mathbf{q}_j), \end{aligned} \tag{B2}$$

where $G = \int d\mathbf{r} g(\bar{\psi} + \sum_{\mathbf{q}\neq\mathbf{0}} a_{\mathbf{q}} e^{i\mathbf{q}\cdot\mathbf{r}+\phi_{\mathbf{q}}}) - g(\bar{\psi})$,

$$\alpha_j = \sum_{k=\max(j,3)}^{N} \left(\frac{(-1)^{k+1}}{k} + \frac{(-1)^k}{k-1} - \tilde{c}^{(k)} \right) \binom{k}{j} \bar{\psi}^{k-j}, \tag{B3}$$

and

$$\beta_{\mathbf{q}_1,\ldots,\mathbf{q}_j} = a_{\mathbf{q}_1} \times \cdots \times a_{\mathbf{q}_j} \cos(\phi_{\mathbf{q}_1} + \cdots + \phi_{\mathbf{q}_j}). \tag{B4}$$

The last term on the right-hand side of Eq. (B2) is the effect of the nonlinearity of ψ higher than ψ^2 on the free-energy functional. Equation (B2) indicates that only the set of wave vectors that satisfy the resonance condition $\sum_j \mathbf{q}_j = \mathbf{0}$ contributes to the free energy functional. The controllable parameters included in this nonlinear effect terms are the correlation functions higher than third order, $\tilde{c}^{(k)}$.

According to Ref. [40] and Eqs. (B2)–(B4), j wave vectors forming a closed loop contribute to the free-energy functional through the ψ^j term with parameter $\tilde{c}^{(k)} (k \geqslant j)$. This suggests that controlling the higher order DCFs decreases the free energy of the competitive patterns. Figure 13 shows the dependency of $\tilde{c}^{(3)}$ and $\tilde{c}^{(4)}$ on the difference in free energy between the CaVO and zigzag lattices in the case that $N = 4$, $\bar{\psi} = 1/4$ and $\theta_1 = \theta_4 = \theta_5 = \theta_6 = 0.8$. Unfortunately, increasing $\tilde{c}^{(3)}$ (or $\tilde{c}^{(4)}$) does not reduce the difference between in free energy between the CaVO and the zigzag lattices. Although decreasing $\tilde{c}^{(3)}$ (or $\tilde{c}^{(4)}$) can reduce the difference in free energy between the CaVO and zigzag lattices, the minimum difference satisfying $F[\psi_{\mathrm{CaVO}}], F[\psi_{\mathrm{zigzag}}] \in \mathbb{R}$ is greater than zero. The results obtained using another values of $(\bar{\psi}, \theta_1 = \theta_4 = \theta_5 = \theta_6)$ have the same trend as seen in Fig. 13. Consequently, suppressing the competitive patterns requires $N > 4$ or a more sophisticated expression for the higher–order DCFs than the local density approximation (e.g., Ref. [8]).

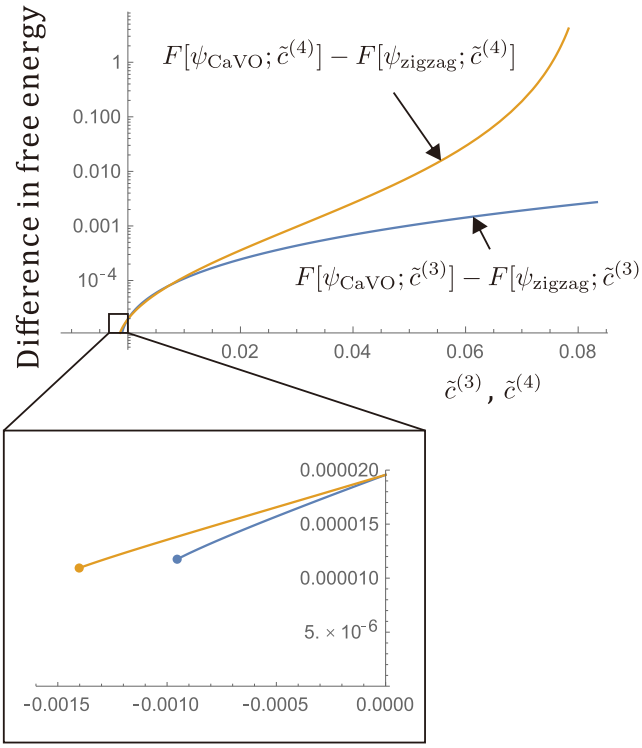

FIG. 13. Analytical result of the dependency of $\tilde{c}^{(3)}$ and $\tilde{c}^{(4)}$ on the difference in the free energy between the CaVO and the zigzag lattices in the case that $\bar{\psi} = 1/4$ and $\theta_1 = \theta_4 = \theta_5 = \theta_6 = 0.8$. The circles indicate the limit satisfying $F[\psi_{\mathrm{CaVO}}], F[\psi_{\mathrm{zigzag}}] \in \mathbb{R}$.

[1] K. R. Elder, M. Katakowski, M. Haataja, and M. Grant, Modeling Elasticity in Crystal Growth, Phys. Rev. Lett. **88**, 245701 (2002).

[2] K. R. Elder and M. Grant, Modeling elastic and plastic deformations in nonequilibrium processing using phase field crystals, Phys. Rev. E **70**, 051605 (2004).

[3] K. R. Elder, N. Provatas, J. Berry, P. Stefanovic, and M. Grant, Phase-field crystal modeling and classical density functional theory of freezing, Phys. Rev. B **75**, 064107 (2007).

[4] M. Greenwood, N. Provatas, and J. Rottler, Free Energy Functionals for Efficient Phase Field Crystal Modeling of Structural Phase Transformations, Phys. Rev. Lett. **105**, 045702 (2010).

[5] M. Greenwood, J. Rottler, and N. Provatas, Phase-field-crystal methodology for modeling of structural transformations, Phys. Rev. E **83**, 031601 (2011).

[6] V. W. L. Chan, N. Pisutha-Arnond, and K. Thornton, Phase-field crystal model for a diamond-cubic structure, Phys. Rev. E **91**, 053305 (2015).

[7] S. K. Mkhonta, K. R. Elder, and Z.-F. Huang, Exploring the Complex World of Two-Dimensional Ordering with Three Modes, Phys. Rev. Lett. **111**, 035501 (2013).

[8] M. Seymour and N. Provatas, Structural phase field crystal approach for modeling graphene and other two-dimensional structures, Phys. Rev. B **93**, 035447 (2016).

[9] S. R. Hall, F. H. Allen, and I. D. Brown, The crystallographic information file (CIF): A new standard archive file for crystallography, Acta Crystallogr. Sect. A **47**, 655 (1991).

[10] T. V. Ramakrishnan and M. Yussouff, First-principles order-parameter theory of freezing, Phys. Rev. B **19**, 2775 (1979).

[11] A. J. Archer, D. J. Ratliff, A. M. Rucklidge, and P. Subramanian, Deriving phase field crystal theory from dynamical density functional theory: Consequences of the approximations, Phys. Rev. E **100**, 022140 (2019).

[12] C. M. Bishop, *Pattern Recognition and Machine Learning* (Springer, New York, 2006).

[13] A. G. Baydin, B. A. Pearlmutter, A. A. Radul, and J. M. Siskind, Automatic differentiation in machine learning: A survey, J. Mach. Learn. Res. **18**, 5595 (2017).

[14] T. Fennell, J. O. Piatek, R. A. Stephenson, G. J. Nilsen, and H. M. Rønnow, Spangolite: An $s = 1/2$ maple leaf lattice antiferromagnet? J. Phys.: Condens. Matter **23**, 164201 (2011).

[15] H. Kageyama, K. Yoshimura, R. Stern, N. V. Mushnikov, K. Onizuka, M. Kato, K. Kosuge, C. P. Slichter, T. Goto, and Y. Ueda, Exact Dimer Ground State and Quantized Magnetization Plateaus in the Two-Dimensional Spin System $SrCu_2(BO_2)_2$, Phys. Rev. Lett. **82**, 3168 (1999).

[16] H. Feng, C. Liu, S. Zhou, N. Gao, Q. Gao, J. Zhuang, X. Xu, Z. Hu, J. Wang, L. Chen *et al.*, Experimental realization

of two-dimensional buckled Lieb lattice, Nano Lett. **20**, 2537 (2020).

[17] S. Taniguchi, T. Nishikawa, Y. Yasui, Y. Kobayashi, M. Sato, T. Nishioka, M. Kontani, and K. Sano, Spin gap behavior of $s = 1/2$ quasi-two-dimensional system CaV_4O_9, J. Phys. Soc. Jpn. **64**, 2758 (1995).

[18] L. Q. Chen and J. Shen, Applications of semi-implicit Fourier-spectral method to phase field equations, Comput. Phys. Commun. **108**, 147 (1998).

[19] M. Abadi, A. Agarwal, P. Barham, E. Brevdo, Z. Chen, C. Citro, G. S. Corrado, A. Davis, J. Dean, M. Devin, S. Ghemawat, I. Goodfellow, A. Harp, G. Irving, M. Isard, R. Jozefowicz, Y. Jia, L. Kaiser, M. Kudlur, J. Levenberg, D. Mané, M. Schuster, R. Monga, S. Moore, D. Murray, C. Olah, J. Shlens, B. Steiner, I. Sutskever, K. Talwar, P. Tucker, V. Vanhoucke, V. Vasudevan, F. Viégas, O. Vinyals, P. Warden, M. Wattenberg, M. Wicke, Y. Yu, and X. Zheng, TensorFlow: Large-scale machine learning on heterogeneous systems, 2015. Software available from tensorflow.org.

[20] E. Edlund, O. Lindgren, and M. N. Jacobi, Designing Isotropic Interactions for Self-Assembly of Complex Lattices, Phys. Rev. Lett. **107**, 085503 (2011).

[21] B. A. Lindquist, R. B. Jadrich, and T. M. Truskett, Communication: Inverse design for self-assembly via on-the-fly optimization, J. Chem. Phys. **145**, 111101 (2016).

[22] W. D. Piñeros, R. B. Jadrich, and T. M. Truskett, Design of two-dimensional particle assemblies using isotropic pair interactions with an attractive well, AIP Adv. **7**, 115307 (2017).

[23] H. Chao and R. A. Riggleman, Inverse design of grafted nanoparticles for targeted self-assembly, Mol. Syst. Des. Eng. **3**, 214 (2018).

[24] W. D. Piñeros, M. Baldea, and T. M. Truskett, Designing convex repulsive pair potentials that favor assembly of kagome and snub square lattices, J. Chem. Phys. **145**, 054901 (2016).

[25] W. D. Piñeros and T. M. Truskett, Designing pairwise interactions that stabilize open crystals: Truncated square and truncated hexagonal lattices, J. Chem. Phys. **146**, 144501 (2017).

[26] R. B. Jadrich, B. A. Lindquist, and T. M. Truskett, Probabilistic inverse design for self-assembling materials, J. Chem. Phys. **146**, 184103 (2017).

[27] S. Whitelam, Minimal Positive Design for Self-Assembly of the Archimedean Tilings, Phys. Rev. Lett. **117**, 228003 (2016).

[28] D. Salgado-Blanco and C. I. Mendoza, Non-additive simple potentials for pre-programmed self-assembly, Soft Matter **11**, 889 (2015).

[29] E. C. Oğuz, A. Mijailović, and M. Schmiedeberg, Self-assembly of complex structures in colloid-polymer mixtures, Phys. Rev. E **98**, 052601 (2018).

[30] W. D. Piñeros, B. A. Lindquist, R. B. Jadrich, and T. M. Truskett, Inverse design of multicomponent assemblies, J. Chem. Phys. **148**, 104509 (2018).

[31] J.-P. Hansen and I. R. McDonald, *Theory of Simple Liquids*, 3rd ed. (Academic, London, 1990).

[32] N. Goldenfeld, B. P. Athreya, and J. A. Dantzig, Renormalization group approach to multiscale simulation of polycrystalline materials using the phase field crystal model, Phys. Rev. E **72**, 020601(R) (2005).

[33] B. P. Athreya, N. Goldenfeld, and J. A. Dantzig, Renormalization-group theory for the phase-field crystal equation, Phys. Rev. E **74**, 011601 (2006).

[34] N. Goldenfeld, B. P. Athreya, and J. A. Dantzig, Renormalization group approach to multiscale modelling in materials science, J. Stat. Phys. **125**, 1015 (2006).

[35] R. Spatschek and A. Karma, Amplitude equations for polycrystalline materials with interaction between composition and stress, Phys. Rev. B **81**, 214201 (2010).

[36] D.-H. Yeon, Z.-F. Huang, K. R. Elder, and K. Thornton, Density-amplitude formulation of the phase-field crystal model for two-phase coexistence in two and three dimensions, Philos. Mag. **90**, 237 (2010).

[37] K. R. Elder, Z.-F. Huang, and N. Provatas, Amplitude expansion of the binary phase-field-crystal model, Phys. Rev. E **81**, 011602 (2010).

[38] Wolfram Research, Inc, Mathematica, Version 11.3, Champaign, IL, 2018.

[39] K. Brugger, Pure modes for elastic waves in crystals, J. Appl. Phys. **36**, 759 (1965).

[40] S. K. Mkhonta, K. R. Elder, and Z.-F. Huang, Emergence of Chirality from Isotropic Interactions of Three Length Scales, Phys. Rev. Lett. **116**, 205502 (2016).